International Journal of Multiphase Flow 35 (2009) 155–162

Contents lists available at ScienceDirect

International Journal of Multiphase Flow

journal homepage: www.elsevier.com/locate/ijmulflow

The effect of bubble-induced liquid flow on mass transfer in bubble plumes

Xiaobo Gong [1], Shu Takagi [*,2], Yoichiro Matsumoto

Department of Mechanical Engineering, The University of Tokyo, 7-3-1, Hongo, Bunkyo-ku, Tokyo 113-8656, Japan

ARTICLE INFO

Article history:
Received 30 December 2007
Received in revised form 29 September 2008
Accepted 5 October 2008
Available online 17 October 2008

ABSTRACT

The use of microbubbles to enhance mass transfer in a compact bubble column has become a valuable topic recently. When the liquid flow induced by the presence of microbubbles is taken into account, the behavior of the microbubbles may differ widely from simple estimations. One example is the change of the residence time, which is determined not only by slip velocity but also the velocity of the surrounding liquid. In the present study the effect of the bubble-induced liquid flow on mass transfer in microbubble plumes is analyzed numerically. A two-way coupling Eulerian–Lagrangian approach is used to simulate oxygen bubble plumes with initial bubble diameters from 100 μm to 1 mm and a maximum local void fraction of less than 2% in compact rectangular tanks. The simulations illustrate that the effect of bubble-induced liquid velocity on the residence time of microbubbles increases with the decrease of initial bubble diameters, and also increases with the reduction of initial water depth. The differences between the concentrated and uniform bubble injections are compared. The results show that the uniform injection of microbubbles provides much better mass transfer efficiency than the concentrated injection, because the bubble-induced liquid flow is suppressed when bubbles are injected uniformly over the entire bottom of the tank.

1. Introduction

Bubble plumes with mass transfer are widely observed in biological, chemical and environmental applications, for which reason there is great value in trying to enhance mass transfer in compact bubble column using microbubbles with minimal energy consumption. Prior to any consideration of the effects of liquid flow, a simple analysis suggests the use of microbubbles, first, because the great amount of contact surface area between the gas and liquid phases enhances mass transfer, and second, longer residence time may be expected because smaller bubbles rise with a lower slip velocity. However, because the residence time of bubbles in a plume is determined not only by the bubbles' slip velocity, but the velocity of the surrounding liquid, the consideration of liquid flow becomes the more important for microbubbles since their motion, due to their lower slip velocity, makes them easier to be affected by the surrounding liquid than larger bubbles. This consideration requires a detailed analysis of the effects of bubble-induced liquid flows, which is important for the design of a compact chemical reactor with microbubble plumes.

Many studies on bubble columns and gravity driven bubble flows have been reviewed by Joshi et al. (2002) and Mudde (2005). The phenomenon that the gravity acts with a non-uniform gas fraction profile in a bubble column to accelerate bubbles in the center of the plume and decelerate bubbles near the walls was initially proposed by Hills (1974), who concluded that the effect of the liquid flow leads to a broad distribution in the residence time of the bubbles. Since then, few quantitative analyses of the effects of bubble-induced liquid velocity on residence time have been reported. Experimental study of the bubble residence time in a bubble column is problematic because of the technical difficulty of tracing a single bubble among tens of thousands in a three-dimensionally transient bubble flow. However, the development of methods for the numerical modeling of bubble plumes and computational techniques has enabled the numerical simulation of bubbly flows and the tracking of individual bubbles.

The Eulerian–Lagrangian approach has been widely applied in the study of the motion of dispersed phase (solid particles, gas bubbles or droplets) in a continuous phase (gas or liquid) from a low to moderate void fraction. Two different treatments on the Eulerian approach side have been reported in studies using the two-way coupling Eulerian–Lagrangian approach. In one of these, the fluid with the dominant volume fraction in the flow field is treated as the continuous phase, and interactions between the two phases are given explicitly as source terms in the momentum equation for the continuous phase. This has been the most popular method adopted in the studies of two-phase flow with the Eulerian–Lagrangian approach (Squires and Eaton, 1990; Elghobashi and

* Corresponding author. Tel.: +81 3 5841 6426; fax: +81 3 3818 0835.
E-mail address: takagi@mech.t.u-tokyo.ac.jp (S. Takagi).
[1] Present address: Organ and Body Scale Team, Computational Science Research Program, RIKEN (The Institute for Physical and Chemical Research), 2-1 Hirosawa, Wako City, Saitama 351-0198, Japan.
[2] Computational Science Research Program, RIKEN.

0301-9322/$ - see front matter © 2008 Elsevier Ltd. All rights reserved.
doi:10.1016/j.ijmultiphaseflow.2008.10.001

Truesdell, 1993; Spelt and Biesheuvel, 1997; Delnoij et al., 1997; Climent and Magnaudet, 1999; Mazzitelli et al., 2003). The other method treats the entire mixture of liquid and bubbles with the Eulerian approach, and solves the motion of the mixture using one set of momentum equation (Murai and Matsumoto, 1998; Druzhinin and Elghobashi, 2001; Sokolichin et al., 2004; Gong et al., 2007). Here the interaction terms between the two phases are canceled out in the momentum equation. This method of two-phase coupling differs from the two-way coupling discussed by Drew (1983) and Zhang and Prosperetti (1994). As noted by Sokolichin et al. (2004), its "weaker" two-way coupling indicates the difference that the interaction terms are not explicitly counted in the momentum equations for the mixture and for bubbles.

Mass transfer inside a bubble plume involves multi-scale phenomena, and the wide distribution of various scales and large bubble numbers (around 10^6) makes direct numerical simulations in these studies impossible with current computing technology. Instead of doing that, the averaged Sherwood number based on the relative motion of bubbles to the surrounding liquid (Clift et al., 1978) is often used to study the mass transfer in bubble plumes. Bauer and Eigenberger (1999) proposed the concept of multi-scale modeling for coupling detailed plume structures with mass transfer. In their study, the time scale of the synthesis reaction for gas and liquid is assumed to be larger than that of the fluctuation of local hydrodynamics but sufficiently faster than that of the large-scale mixing in the plume. Whereas Bauer & Eigenberger used the Eulerian–Eulerian approach, Darmana et al. (2005) and Gong et al. (2007) simulated the mass transfer in bubble plumes by tracking each bubble individually with the Eulerian–Lagrangian approach, in which the information of each bubble, such as velocity, diameter and location, is used for the calculation of mass transfer rate directly to give a better resolution.

In this study, the effect of the bubble-induced liquid flow on residence time and mass transfer efficiency is analyzed with the Eulerian–Lagrangian approach. In Section 2, the mathematical model for the present problem is introduced. In Section 3, the numerical results are presented. The effects of the induced flow with different initial bubble sizes and water depths are analyzed, and the effect of bubble injection methods is discussed. Section 4 presents conclusions.

2. Governing equations

2.1. Mathematical model of the bubble plume with Eulerian–Lagrangian approach

In this study, a two-way coupling Eulerian–Lagrangian approach is used to simulate bubble plumes with mass transfer. Details of the governing equations are presented in our previous work (Gong et al., 2007), and summarized briefly as follows.

In the present simulations, the following continuity and momentum equations for the mixture of liquid and bubbles are used

$$\frac{\partial(f_L\rho_L)}{\partial t}+\nabla\cdot(f_L\rho_L\mathbf{u}_L)=0, \tag{1}$$

$$\frac{\partial(f_L\rho_L\mathbf{u}_L)}{\partial t}+\nabla\cdot(f_L\rho_L\mathbf{u}_L\mathbf{u}_L) = -\nabla p+\nabla\cdot\mu_e\left\{\nabla\mathbf{u}_L+(\nabla\mathbf{u}_L)^T-\frac{2}{3}\mathbf{I}\nabla\cdot\mathbf{u}_L\right\}+f_L\rho_L\mathbf{g}, \tag{2}$$

where the density of the gas phase is assumed to be much smaller than that of the liquid phase and so is neglected; f_L is the volume fraction of liquid; μ_e is the effective viscosity of the mixture of the liquid and bubbles as a dilute suspension, which is given as $\mu_e=(1+2.5f_G)\mu_L$ in the case of sufficiently contaminated bubbles which behave like solid particles (Batchelor, 1967). It is noted that, in the present method, two-way coupling is conducted through the pressure Poisson equation with the constraint of continuity equation for the mixture $\nabla\cdot(f_L\mathbf{u}_L+f_G\mathbf{u}_G)=0$ (see Appendix A for more details). This gives the coupling in the momentum equation through the pressure term, although the interaction terms do not appear explicitly in the momentum equation.

The translational motion of individual bubbles is tracked using the following equation

$$\frac{d\mathbf{v}_{b,k}}{dt}=3\frac{D_L\mathbf{u}_L}{Dt}-2\mathbf{g}-\frac{3C_D}{2d_k}|\mathbf{v}_{b,k}-\mathbf{u}_L|(\mathbf{v}_{b,k}-\mathbf{u}_L), \tag{3}$$

where $\boldsymbol{v}_{b,k}$ and d_k are the velocity and diameter of the kth bubble. The subscript b denotes bubble. The buoyancy force, the inertial force due to liquid acceleration, the added-mass force and drag force are taken into account. In Eq. (3), lift force is neglected since it is substantially small compared to other forces in the present simulation when heavily contaminated microbubbles are assumed (Fukuta et al., 2008). The history force is also neglected because it does not show significant contribution as long as the bubbles are not exposed to a sufficiently large pressure gradient (Takagi and Matsumoto, 1996; Takemura and Magnaudet, 2004).

In Eq. (3), the added-mass coefficient of 0.5 has been used; the drag coefficients for solid spheres, as summarized in Table 5.2 in Clift et al. (1978), which were proposed by Oseen (1910) for $Re_b \leqslant 0.1$, Beard (1971) for $0.1 < Re_b \leqslant 20$, and Clift et al. (1978) for $20 < Re_b \leqslant 260$, respectively, are adopted according to different bubble Reynolds numbers

$$C_D=\begin{cases}\frac{24}{Re_b}\left(1+\frac{3}{16}Re_b\right), & Re_b\leqslant 0.01\\ \frac{24}{Re_b}\left(1+0.1315Re_b^{(0.82-0.05\log_{10}Re_b)}\right), & 0.01<Re_b\leqslant 20\\ \frac{24}{Re_b}\left(1+0.1935Re_b^{0.6305}\right), & 20<Re_b\leqslant 260\end{cases} \tag{4}$$

where $Re_b=\rho_L d|\mathbf{v}_b-\mathbf{u}_L|/\mu_L$.

Bubble position is calculated explicitly as

$$\mathbf{X}_{b,k}(t)=\mathbf{X}_{b,k}(0)+\int_0^t\mathbf{v}_{b,k}(\tau)d\tau. \tag{5}$$

The void fraction of bubbles in grid scale is evaluated by

$$f_G=\frac{1}{V_L}\sum_{k=1}^{N_b}\left(\omega_k\frac{\pi d_k^3}{6}\right),\quad\text{and}\quad f_L=1-f_G, \tag{6}$$

where V_L is the volume of the computational cell, i.e. the control volume for the descretization; N_b is the number of bubbles in the control volume; ω_k is the weighting function which indicates the distance weight of the kth bubble from the center of the bubble to the center points of the control volume. The method used to calculate the weighting function ω_k is the same as that proposed in Delnoij et al. (1999).

In this study, in order to capture the detailed plume structures we use high order central difference scheme (Morinishi et al., 1998) to exclude numerical viscosities and a dense grid to discretize the flow field. $40\times40\times40$ grid points are used for the simulation of $0.1\times0.1\times0.1$ m^3 water tank, by which grid density the grid independence of the time-averaged properties of the numerical results was confirmed and the present Eulerian–Lagrangian approach was validated through reproducing the detailed plume structure of 130 μm bubbles (Alam and Arakeri, 1993) as shown in our previous study (Gong et al., 2007). In this study, stable numerical results were obtained without introducing the numerical viscosity and turbulent models. The fluctuations smaller than the grid scale in the flow field are not resolved at the present stage so that our simulations are more valuable for showing the differences in various conditions than predicting the absolute quantities.

2.2. Model for mass transfer in bubble plumes

The mass loss due to gas dissolution is formulated as

$$j_b = -\frac{d}{dt}\left(\frac{\pi d^3}{6}\rho_G\right) = \pi d^2 k(c_b - c_\infty), \tag{7}$$

where k is the mass transfer coefficient; c_b is the concentration inside the bubble; and c_∞ is that in the surrounding liquid. In the present study, the mass transfer rate of each bubble is evaluated using the averaged Sherwood number of the bubble. Using the definition of the Sherwood number $Sh_b = kd/\mathcal{D}$, where $\mathcal{D}$ is the molecular diffusion coefficient, Eq. (8) is given as

$$j_b = \pi d Sh_b \mathcal{D}(c_b - c_\infty), \tag{8}$$

where the averaged Sherwood number Sh_b is calculated using the Reynolds and Peclet numbers (Clift et al., 1978) where

$$Sh_b = 1 + (Pe_b + 1)^{1/3} Re_b^{0.077}, \tag{9}$$

and where $Pe_b = d|\mathbf{v}_b - \mathbf{u}_L|/\mathcal{D}$. Eq. (9) is available for a solid sphere in the range of $1 \leqslant Re_b \leqslant 400$. The concentration c_∞ in Eq. (8) is calculated by a 3rd order Lagrangian interpolation with the concentration (on the grid scale) in the surrounding liquid to the location of the bubble. The concentration inside bubble c_b in Eq. (8) is calculated with the equilibrium assumption of concentration over a liquid and gas interface using Henry's Law as

$$c^* = \alpha \frac{p_b}{\mathcal{H}}, \tag{10}$$

where p_b is the pressure in the bubble and α is the mole fraction of the soluble gas. Proper utilization of the units is important for this equation, a discussion of which may be found in Sander (1999). The units used here are *mol per mol* for c^*, *Pa per mol-fraction* for $\mathcal{H}$, and *Pa* for p_b. The surface tension effect with a surface tension coefficient σ, is considered when the pressure inside bubble is calculated, as

$$p_b = p_L(\mathbf{x}_b) + \frac{4\sigma}{d}. \tag{11}$$

Bubble diameter changes corresponding to the loss of mass and change of pressure in the bubble. The experiment by Takemura and Yabe (1999) showed that diameter change due to pressure variation inside a bubble by a translational motion is much smaller, and negligible when compared with the effect of mass loss. The following equation is used to calculate the diameter change:

$$\dot{d} \approx \frac{2j_b}{\pi d^2 \rho_G}. \tag{12}$$

On the grid scale, the source term for the concentration equation is given by averaging the dissolution rates of all bubbles in the control volume as

$$S_L = \frac{1}{V_L}\sum_{k=1}^{N_b}(\omega_k j_k), \tag{13}$$

where ω_k is the same distance weighting function as in Eq. (6). The transportation equation for the concentration of the dissolved gas is

$$\frac{\partial}{\partial t}(f_L c_L) + \nabla\cdot(f_L c_L \mathbf{u}_L) = \nabla\cdot[\mathcal{D}\nabla(f_L c_L)] + S_L. \tag{14}$$

More details on boundary conditions used in the present simulation, such as free surface boundary on the top of the bubble column, were explained in detail in our previous work (Gong et al., 2007).

3. Numerical results and discussion

A compact rectangular water tank is introduced in the present simulations for the oxygen microbubble plumes. The tank has a square cross-section in the horizontal plane, 0.1 m on each side. Water depths H_0 are initially set as 0.1 m and 0.4 m in order to check the effect of bubble-induced liquid velocity at different initial water depths. The depth of 0.1 m is not representative of most practical utilizations, such as where larger bubbles of 3–5 mm in diameter or greater are often used; but when microbubbles are introduced, e.g., 100 μm bubbles, 0.1 m becomes a realistic water depth for a compact chemical reactor (Gong et al., 2007).

The initial bubble diameter for each plume is set uniformly within the range of 100 μm to 1 mm. The oxygen supply rate is fixed at 10^{-8} m^3/s and the maximum void fraction at the bubble injection region is less than 2%. Two different bubble injection methods are used in the present simulations, concentrated and uniform. For the concentrated method, an injection region of 0.01 m square area is set at the center of the tank bottom, and bubbles are randomly released over the entire injection area. For the uniform method, the injection region is set as the entire bottom of the tank. In this study, microbubbles are assumed to be at terminal velocity at injection, which is a reasonable assumption since a rising bubble reaches its terminal velocity soon from the rest state within the height of several bubble diameters (Zhang and Finch, 2001).

The physical and chemical properties of oxygen and the liquid we used are summarized in Table 1.

The numerical algorithm is given in Appendix A. $40 \times 40 \times 40$ grid points are used for the simulation of $0.1 \times 0.1 \times 0.1$ m^3 water tank. The time step is decided based on the smaller one of the time scales for the diffusion stability $\tau_1 < \frac{\Delta^2}{2\mu}$ (where Δ is the grid length) and the relaxation of the translational motion of a bubble $\tau_2 = \frac{2d^2 Re_b}{3C_D\mu}$. Using these parameter sets, stable numerical solutions are achieved.

3.1. The effect of initial bubble diameter for different initial water depths

Fig. 1 shows the plume profile, liquid velocity and concentration contours of dissolved oxygen in the tank when the initial water depth equals 0.1 m. As shown in the figures, bubbles are concentrated in the center of the plume. The non-uniform presence of bubbles induces an upward flow of liquid due to the buoyancy effect; as the liquid in this region flows in the same direction as the rising bubbles, the bubbles are lifted by the surrounding liquid. The concentration contours show that the dissolution of oxygen in the plume with smaller bubbles is more efficient than that with larger ones.

Differences in plumes with the same initial bubble diameter (200 μm) but different water depths (0.1 and 0.4 m) are shown in Fig. 2. The plume in 0.4 m water depth has more space for the dispersion of bubbles with the development of the bubble-induced liquid flow than the plume confined to 0.1 m depth. Spatial variations in liquid flow and the dispersion of bubbles from the center of the plume reduce the local void fraction and attenuate the buoyancy effect. As indicated by the velocity distribution and stream lines of the averaged liquid flow field, the circulation induced in

Table 1
The properties of liquid and gas considered in this study[a].

ρ_L, density of liquid [kg/m^3]	998.2 (Water)
ρ_G, density of gas [kg/m^3]	1.331 (Oxygen)
μ_L, dynamic viscosity of water [Pa s]	1.002×10^{-3}
σ, surface tension coefficient of water [N/m]	72.75×10^{-3}
$\mathcal{D}$, molecular diffusion coefficient of oxygen in water[b] [m^2/s]	2.37×10^{-9}
$\mathcal{H}$, Henry's Law constant[c] for Oxygen [Pa mol/mol]	4.357×10^9

[a] The system is at 20 °C and 1 atm = 101,325 Pa.
[b] Data from Reid et al. (1977) & Wilke–Chang Estimation Method (1955).
[c] Data from Corbitt (1999).

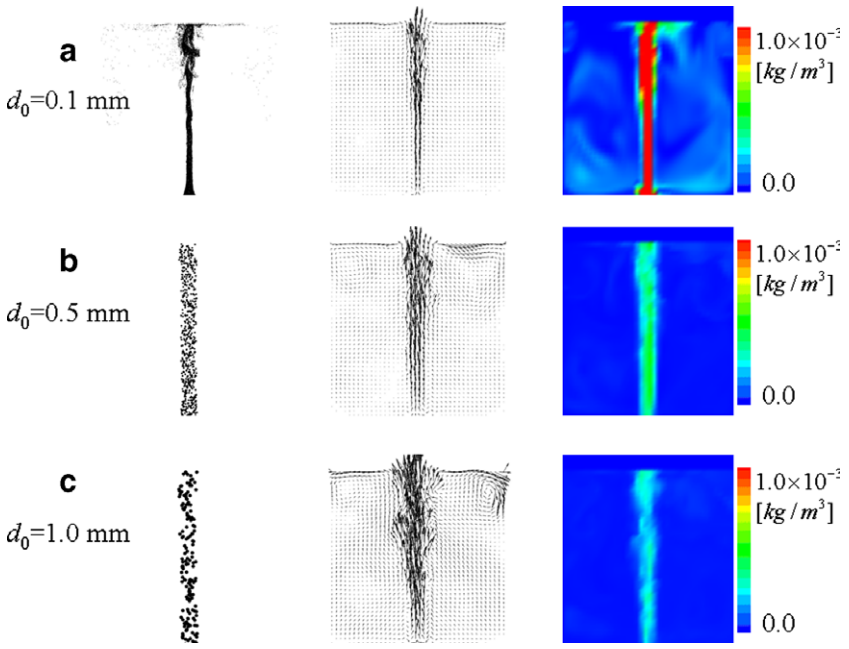

Fig. 1. Snapshots of bubble plume profiles, liquid velocity and the concentration contours of dissolved oxygen in the central plane of the oxygen bubble plumes with different initial bubble diameters (t = 60 s, H_0 = 0.1 m; (a) d_0 = 0.1 mm; (b) d_0 = 0.5 mm; (c) d_0 = 1.0 mm).

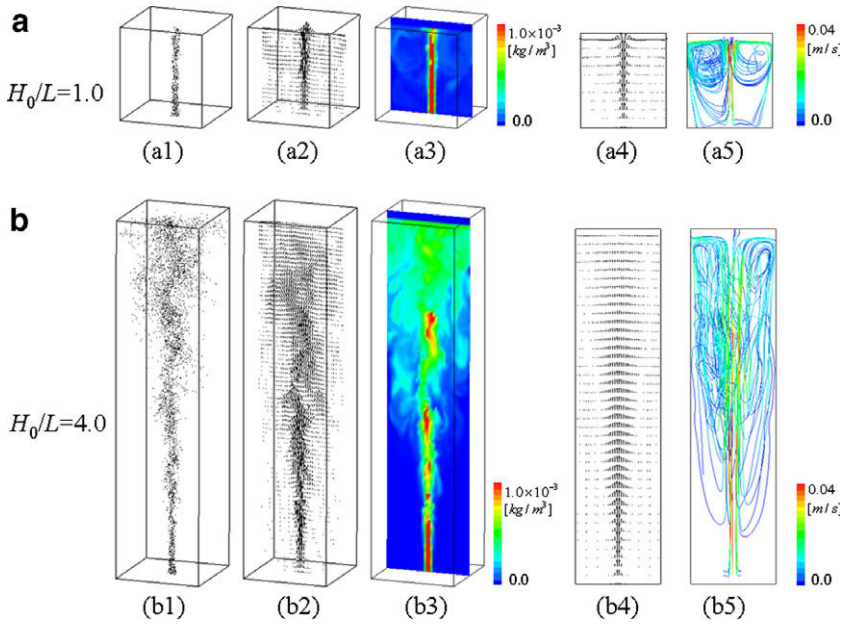

Fig. 2. The effect of the initial water depth on the bubble plumes with mass transfer (d_0 = 0.2 mm). From left to right figures are, respectively: snapshots at 60.0 s which are (1) plume profiles (2), the velocity field of the liquid phase (3), the concentration contour in the central plane of dissolved gas; and (4) and (5) are the averaged liquid velocity of the well developed flow field in the central plane, and the stream lines of the averaged liquid flow field contoured with the module of averaged liquid velocity.

the lower water depth is less complex. The greater water depth exhibits increased circulation with greater fluctuations.

We evaluate the terminal velocity of a bubble from the balance of drag force and buoyancy as

$$v_{b,0} = \left(\frac{4d_0 g}{3C_D}\right)^{1/2}, \tag{15}$$

where the subscript 0 denotes the initial state. The averaged bubble velocity up to the surface of the water is normalized by this terminal velocity and shown in Fig. 3a and b, respectively, for 0.1 and 0.4 m water depths. Fig. 3a shows that the averaged velocity of bubbles is larger than the initial terminal velocity because of the bubble-induced liquid flow. In the plume with 1mm bubbles, the bubble velocity is less than twice terminal velocity, which indicates that the slip velocity is larger than the induced liquid velocity. However, in the plume with 100 μm bubbles, the maximum induced liquid velocity is around 10 times greater than the terminal velocity. Fig. 3b shows that with a greater water depth, the maximum bubble velocity in the plume with 100 μm bubbles also exceeds 10 times terminal velocity, though as the flow develops, velocity decreases, and even falls below initial terminal velocity due to bubble shrink-

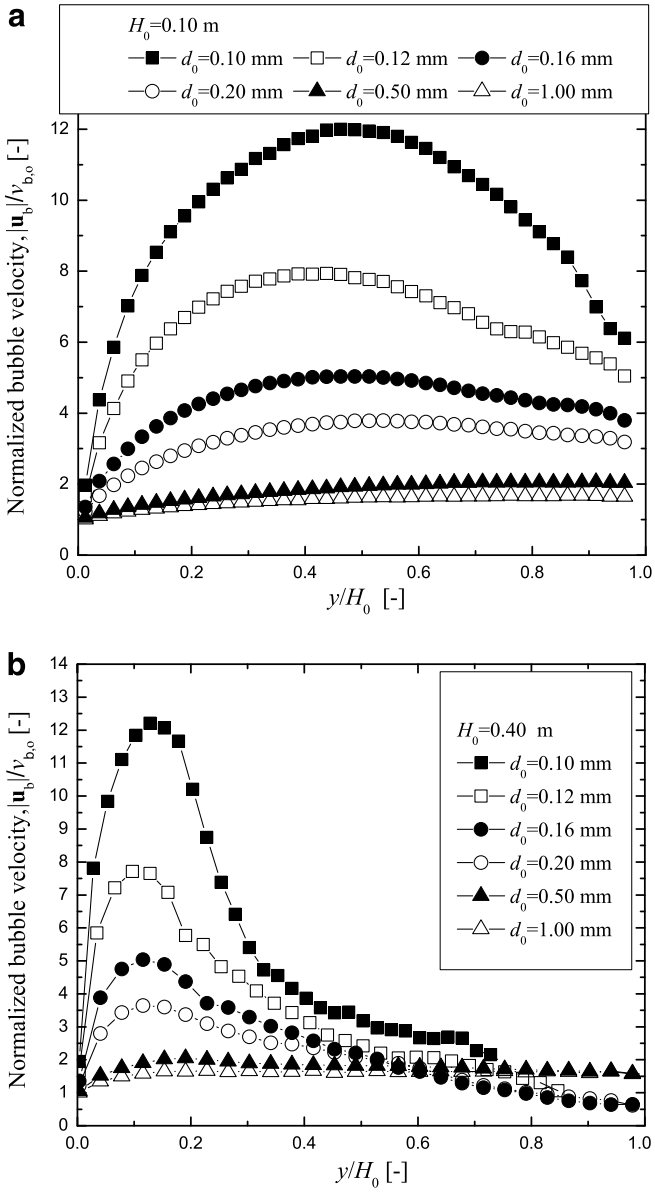

Fig. 3. The normalized bubble velocity up to the surface of the water ((a) H_0 = 0.1 m; (b) H_0 = 0.4 m; $v_{b,0}$ is the terminal velocity of a single bubble, $v_{b,0} = (\frac{4d_0 g}{3C_D})^{1/2}$).

age with the dissolution of gas as the bubbles rise. Fig. 3 indicates that the smaller the initial bubble size is, the greater the effect of bubble-induced liquid velocity on rising velocity of bubbles, and this effect of the induced velocity is more obvious for the plume in a lower water depth.

Eq. (16) gives an estimation of the residence time of an isolated bubble without considering the effect of bubble-induced flow as

$$t^* = H_0\left(\frac{4d_0 g}{3C_D}\right)^{-1/2}, \tag{16}$$

where H_0 is the initial water depth. Normalized by t^*, the averaged residence time of bubbles in plumes is shown in Fig. 4. For plumes in the 0.4 m water depth with bubbles smaller than 200 μm, no residence times are shown because in the present simulations for these cases the oxygen bubbles dissolve efficiently and most of them disappear before reaching the water surface. Fig. 4 shows that the averaged residence time in plumes becomes smaller than the estimated value, t^*, due to the effect of the induced flow. In the plumes

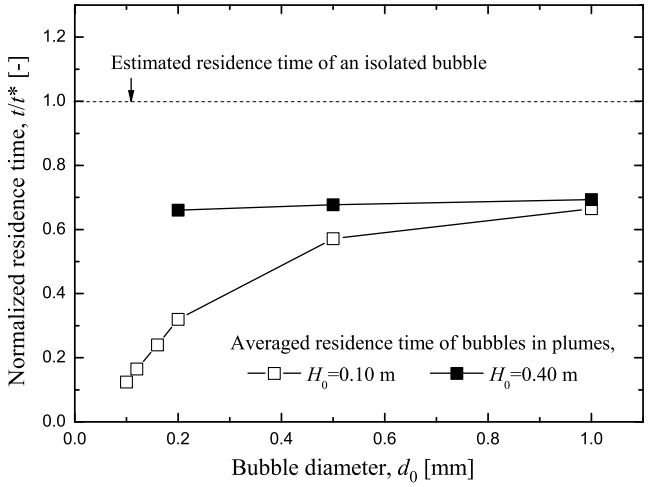

Fig. 4. The normalized residence time of bubbles with different initial bubble diameters and initial water depths (t^* is the estimated residence time of an isolated bubble, $t^* = H_0(\frac{4d_0 g}{3C_D})^{-1/2}$).

with 0.1 m water depth, the residence time for 1 mm bubbles is about 70% of the estimated value, while for 100 μm bubbles, it is only about 10% of the estimated value. This result suggests that the dependence of the averaged residence time on the induced velocity increases as initial bubble size decreases. The residence time in 0.4 m water depth does not decrease sharply with the decrease of initial bubble size as shown in 0.1 m water depth, which reveals that the dependence of bubble residence time on bubble-induced liquid velocity is higher at the lower initial depth.

Fig. 5 shows the oxygen dissolution efficiency in the bubble plumes. Here, dissolution efficiency is defined as the ratio of the amount of gas dissolved q_{dis} to the amount of gas injected q_{inj}. Eq. (17) is proposed as the estimated dissolution efficiency of an isolated bubble with negligible diameter change (see Appendix B for details):

$$E_{fi} = \frac{q_{dis}}{q_{inj}} = 1 - \exp\left\{-3\sqrt{3}\,\frac{\rho_L T\mathcal{R}\mathcal{D}}{M_L g^{1/2}\mathcal{H}} Sh_b h C_D^{1/2} d_0^{-5/2} 10^3\right\}, \tag{17}$$

where $\mathcal{R}$ is the universal gas constant; T is the temperature of the system; M_L is the molecular weight of the liquid. As shown in Fig. 5, the dissolution efficiency of the plume with 1 mm bubbles

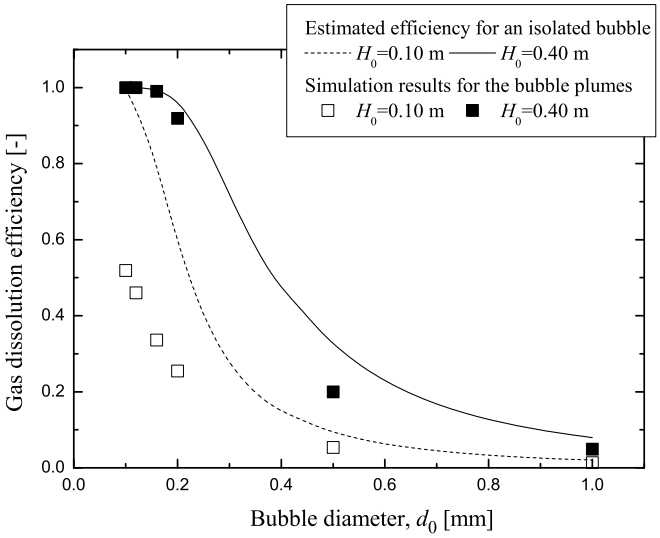

Fig. 5. Oxygen dissolution efficiency in bubble plumes (the estimated value for an isolated bubble is $E_{fi} = \frac{q_{dis}}{q_{inj}} = 1 - \exp\{-3\sqrt{3}\,\frac{\rho_L T\mathcal{R}\mathcal{D}}{M_L g^{1/2}\mathcal{H}} Sh_b h C_D^{1/2} d_0^{-5/2} 10^3\}$).

is almost the same as the estimated value, but efficiency in the 0.1 m water depth cases increases more slowly than the estimated value as initial bubble diameter is reduced. This is because as initial bubble size falls, residence time becomes more dependent on bubble-induced liquid velocity than slip velocity, resulting in a dramatic reduction in residence time and a clear reduction in mass transfer efficiency. Fig. 5 also shows that efficiencies are closer to the estimated value with initial bubble diameters smaller than 200 μm at the 0.4 m depth than at 0.1 m, and decreased mass transfer efficiency due to acceleration from bubble-induced liquid flow is more obvious in the 0.1 m depth.

These results are problematic for industrial applications. Expectations for microbubbles have included improved mass transfer efficiency and lower operation costs as a result of smaller tank sizes. Unfortunately, smaller tank sizes and microbubbles bring about lower bubble residence time and mass transfer efficiency due to the increased dominance of bubble-induced liquid velocity, a problem which provides more than sufficient motivation to continue detailed analyses on bubble injection methods.

3.2. The effect of bubble injection method

In this section analysis is confined to the 0.1 m water depth, the target tank reduction size of this study, with simulations comparing bubble flows of uniform and concentrated injection.

The plume profiles, velocity of liquid fields and the concentration contours of dissolved oxygen are shown from left to right, respectively, in Fig. 6. When bubbles are injected uniformly, they distribute more uniformly throughout the tank and bubble-induced liquid velocity is much smaller than with concentrated injection, and the concentration distribution of the dissolved oxygen is uniform. Higher concentration is observed near the bottom because more gas dissolves and accumulates there.

The averaged rising velocities of bubbles with uniform injection normalized with terminal velocity are shown in Fig. 7. These differ greatly from bubble behaviors exhibited in concentrated injection shown in Fig. 3, as there was no acceleration. Fig. 7 shows that the bubbles decrease in velocity as they rise due to shrinkage with gas dissolution.

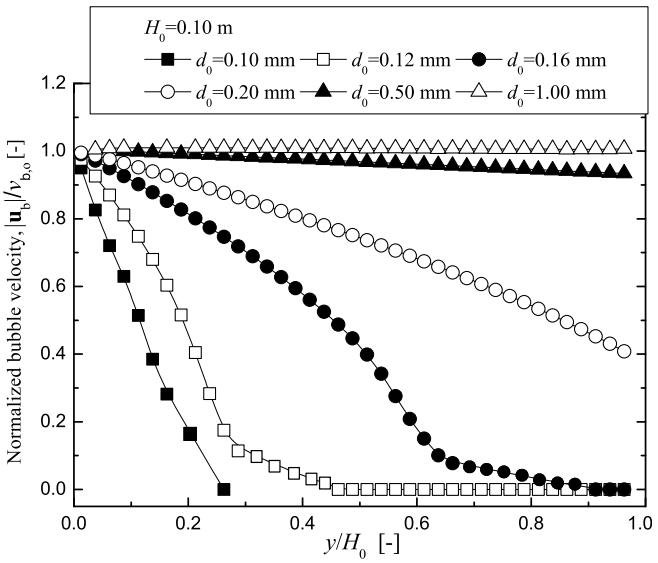

Fig. 7. The normalized bubble velocity up to the surface of the water with uniform injection in the entire bottom area (H_0 = 0.1 m; $v_{b,0}$ is the same estimated velocity as used in Fig. 3).

Absent bubble-induced liquid velocity, residence time with uniform bubble injection becomes more dependent on slip velocity. As shown in Fig. 8, residence time for concentrated injection is always smaller than estimated residence time, t^*, whereas with uniform injection residence time increases, and even exceeds the estimated value due to the fact that decreased slip velocity as a result of bubble shrink was not considered.

A comparison of mass transfer efficiency between the two bubble injection methods is shown in Fig. 9. Dissolution efficiency with concentrated bubble injection is always lower than that estimated using Eq. (17), whereas it increases with uniform bubble injection. Fig. 9 reveals that governing velocity with uniform bubble injection is slip velocity, vice induced liquid velocity, as in the case with concentrated injection.

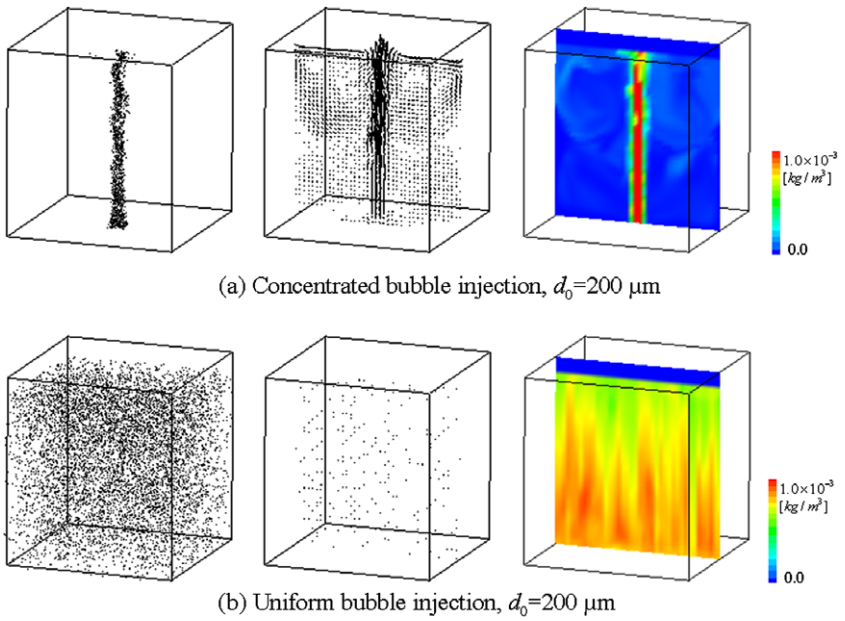

Fig. 6. The comparison of the oxygen bubble plumes with different bubble injection methods. Snapshots from the left to right are, respectively: bubble plume profiles, liquid velocity and the concentration contours of dissolved oxygen in the central plane ((a) with concentrated injection in the center of the bottom; (b) with uniform injection in the entire bottom area; t = 60 s, H_0 = 0.1 m, d_0 = 200 μm).

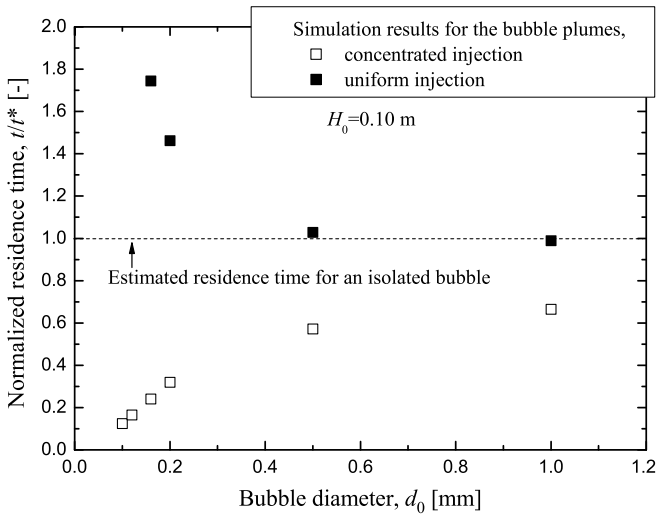

Fig. 8. The comparison of the averaged residence times of bubbles with concentrated injection in the center of the bottom and uniform injection in the entire bottom area (H_0 = 0.1 m; t^* is the same estimated value as used in Fig. 4).

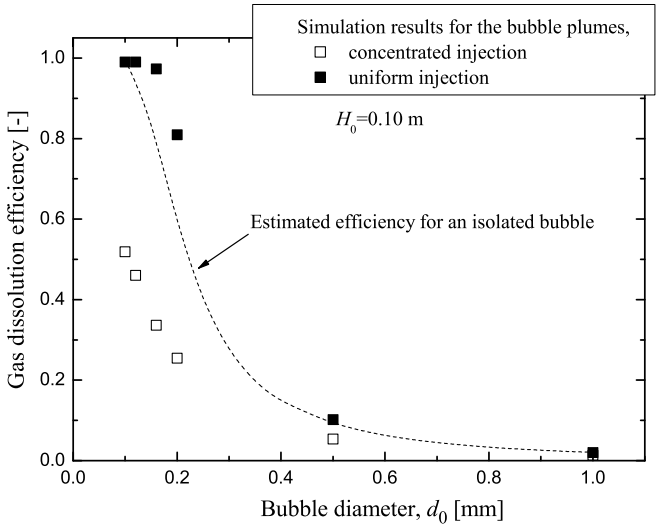

Fig. 9. The comparison of the mass transfer efficiency with concentrated injection in the center of the bottom and uniform injection in the entire bottom area (H_0 = 0.1 m; the estimated value for an isolated bubble is the same as used in Fig. 5).

These analyses show that the uniform bubble injection over the entire bottom of the tank results in much less induced flow, which provides much better mass transfer efficiency than that offered by concentrated injection. They confirm quantitatively that spatially uniform injection of a microbubble column is the more effective way to avoid high induced velocity and achieve efficient gas dissolution.

4. Conclusion

In this study, bubble plumes were simulated with a two-way coupling Eulerian–Lagrangian approach. The effects of bubble-induced liquid flow on the residence time of the bubbles and gas dissolution efficiency with different initial bubble diameters, water depth and bubble injection methods were investigated.

The numerical results show that with the decrease of the initial bubble diameter in a plume, residence time and dissolution efficiency become more dependent on bubble-induced liquid velocity rather than slip velocity. This negative effect of bubble-induced liquid flow is more conspicuous in microbubble plumes confined in a compact water tank with concentrated bubble injection.

The analyses for the comparison of bubble flows with uniform and concentrated injections show that the concentrated injection method increases bubble-induced liquid velocity, and thus reduced mass transfer efficiency. While endeavors toward generating and using microbubbles efficiently are valuable, a high local concentration of bubbles in the plume must be avoided in order to achieve higher mass transfer efficiency. The present study proposes that reduced bubble size makes the injection method a critical matter, and that uniform injection has been shown to offer much better performance than concentrated injection.

Acknowledgements

This work is supported by the NEDO Grant Program of Japan under the project ID 04A20004. Authors would like to thank Mr. David W. Chapmon for helping us to prepare the manuscript of this paper.

Appendix A. The present numerical algorithm for simulations of bubble plume with mass transfer

The governing equations of the present two-way coupling Eulerian–Lagrangian approach for bubble plume with mass transfer are shown as Eqs. (1) and (14). The following algorithm is used in solving the governing equations.

1. Calculate $\mathbf{u}_G^{N+1}$, $\mathbf{X}_G^{N+1}$ with the known $\mathbf{u}_G^N$, $\mathbf{u}_L^N$ and d^N according to Eqs. (3) and (5).
2. Get f_G^{N+1} at $\mathbf{X}_G^{N+1}$ according to Eq. (6).
3. Get the projection speed of the continuous phase $\mathbf{u}_L^*$ with the fractional step method according to Eq. (2) that

$$\mathbf{u}_L^* = \mathbf{u}_L^N + \Delta t\left\{\frac{3}{2}\left(A^N + B^N\right) - \frac{1}{2}\left(A^{N-1} + B^{N-1}\right) + \mathbf{g}\right\},$$

$$\text{where } A = -\mathbf{u}_L \cdot \nabla \mathbf{u}_L \text{ and } B = \frac{1}{f_L^{N+1}}\nabla \cdot \mu_e\left\{\nabla \mathbf{u}_L + (\nabla \mathbf{u}_L)^T - \frac{2}{3}\mathbf{I}\nabla \cdot \mathbf{u}_L\right\}.$$

4. Calculate $D^* = \frac{1}{\Delta t}\nabla \cdot (f_L^{N+1}\mathbf{u}_L^*) - \frac{f_G^{(N+1)} - f_G^{(N)}}{(\Delta t)^2}$ accounting the continuity of the mixture with Eq. (1).
5. Solve pressure Poisson equation $\nabla^2 p^{(N+1)} = D^*$.
6. Correction of the velocity of liquid phase: $\mathbf{u}_L^{N+1} = \mathbf{u}_L^* - \frac{\Delta t}{f_L^{N+1}}\nabla p^{N+1}$.
7. Calculate j_b^{N+1} with known $\mathbf{u}_G^{N+1}, \mathbf{u}_L^{N+1}, p^{N+1}, d^N$ and c_L^N according to Eq. (8).
8. Get d^{N+1} according to Eq. (12).
9. Calculate S_L^{N+1} and c_L^{N+1} according to Eqs. (13) and (14).
10. Continue step 1 for the calculation of the next time step.

Appendix B. An estimation of dissolution efficiency for an rising bubble with negligible diameter change

Calculating the mass transfer rate across the surface area of a spherical bubble

$$j_b = -\frac{d}{dt}\left(\frac{\pi d^3}{6}\rho_G\right) = \pi d^2 k(c_b - c_\infty), \tag{7}$$

using the ideal gas law $\rho_G = \frac{p_G}{T\mathcal{R}}$ and Henry's law $c = \frac{p_G}{\mathcal{H}}\frac{\rho_L}{M_L}10^3$, and the assumption that the diameter change along bubble rising is negligible, we obtained

$$\frac{dp_G}{dt} = -\frac{6\rho_L T\mathcal{R}}{d_0 M_L \mathcal{H}}k(p_G - p_\infty)10^3, \tag{A1}$$

where the initial condition is $p_{G,0} = p_L(x_0) + 4\sigma/d_0$ when t=0.

As a solution of Eq. (A1), the change of the partial pressure of soluble gas inside the bubble is calculated as

$$p_G = p_\infty + p_{G,0}\exp\left\{-\frac{6\rho_L T\mathcal{R} d_0 M_L \mathcal{H}}{k}t10^3\right\}. \tag{A2}$$

Thus, the concentration of soluble gas inside the bubble is expressed using the Henry's law as

$$c = c_\infty + c_0\exp\left\{-\frac{6\rho_L T\mathcal{R}}{d_0 M_L \mathcal{H}}kt10^3\right\}, \tag{A3}$$

where $c_\infty = \frac{\rho_L}{M_L}\frac{p_\infty}{\mathcal{H}}10^3$ and $c_0 = \frac{\rho_L}{M_L}\frac{p_{G,0}}{\mathcal{H}}10^3$.

The amount of gas dissolved from the bubble with negligible diameter change within a rising period of t_b is integrated as

$$\begin{aligned} q_{dis} &= \int_0^{t_b} j d\tau = \int_0^{t_b} \pi d^2 k(c - c_\infty)d\tau \\ &= \pi d_0^2 k\frac{p_{G,0}}{\mathcal{H}}\frac{\rho_L}{M_L}10^3\int_0^{t_b}\exp\left\{-\frac{6\rho_L T\mathcal{R}}{d_0 M_L\mathcal{H}}kt10^3\right\}d\tau \\ &= \frac{\pi d_0^3}{6}\frac{p_{G,0}}{T\mathcal{R}}\left(1-\exp\left\{-\frac{6\rho_L T\mathcal{R}}{d_0 M_L\mathcal{H}}kt_b10^3\right\}\right). \end{aligned} \tag{A4}$$

Placing the relation of $Sh_b = kd/\mathcal{D}$ into Eq. (A4) for the mass transfer efficient k, and estimate t_b, similar to Eq. (16), with $t_b = h\left(\frac{4d_0 g}{3C_D}\right)^{-1/2}$, q_{dis} is calculated as

$$q_{dis} = \frac{\pi d^3}{6}\frac{p_{G,0}}{T\mathcal{R}}\left(1-\exp\left\{-3\sqrt{3}\frac{\rho_L T\mathcal{R}\mathcal{D}}{M_L g^{1/2}\mathcal{H}}Sh_b h C_D^{1/2} d_0^{-5/2}10^3\right\}\right); \tag{A5}$$

noting that the initial amount of gas injected in the bubble is

$$q_{inj} = \rho_G\frac{\pi d_0^3}{6} = \frac{p_{G,0}}{T\mathcal{R}}\frac{\pi d_0^3}{6}, \tag{A6}$$

while the efficiency for an isolated bubble with negligible diameter change is estimated as

$$E_{fi} = \frac{q_{dis}}{q_{inj}} = 1-\exp\left\{-3\sqrt{3}\frac{\rho_L T\mathcal{R}\mathcal{D}}{M_L g^{1/2}\mathcal{H}}Sh_b h C_D^{1/2} d_0^{-5/2}10^3\right\}. \tag{17}$$

References

Alam, M., Arakeri, V.H., 1993. Observations on transition in plane bubble plumes. J. Fluid Mech. 254, 363–374.

Batchelor, G.K., 1967. An Introduction to Fluid Dynamics. Cambridge University Press, Cambridge, UK.

Bauer, M., Eigenberger, G., 1999. A concept for multi-scale modelling of bubble columns and loop reactors. Chem. Eng. Sci. 54, 5109–5117.

Beard, K.V., 1971, Ph.D. Thesis, University of California, Los Angeles.

Clift, R., Grace, J.R., Weber, M.E., 1978. Bubbles, Drops and Particles. Academic Press, New York. p26, p112, p121.

Climent, E., Magnaudet, J., 1999. Large-scale simulation of bubble-induced convection in a liquid layer. Phys. Rev. Lett. 82 (24), 4827–4830.

Corbitt, R.A., 1999. Standard Handbook of Environmental Engineering. McGraw-Hill Inc. pp. 5.154–5.155.

Darmana, D., Deen, N.G., Kuipers, J.A.M., 2005. Detailed modelling of hydrodynamics, mass transfer and chemical reactions in a bubble column using a discrete bubble model. Chem. Eng. Sci. 60 (12), 3383–3404.

Delnoij, E., Lammers, F.A., Kuipers, J.A.M., van Swaaij, W.P.M., 1997. Dynamic simulation of dispersed gas–liquid two-phase flow using a discrete bubble model. Chem. Eng. Sci. 52, 1429–1458.

Delnoij, E., Kuipers, J.A.M., van Swaaij, W.P.M., 1999. A three-dimensional CFD model for gas–liquid bubble columns. Chem. Eng. Sci. 54, 2217–2226.

Drew, D.A., 1983. Mathematical modeling of two-phase flow, *Ann.* Rev. Fluid Mech. 15, 261–291.

Druzhinin, O.A., Elghobashi, S.E., 2001. Direct numerical simulation of a three-dimensional spatially developing bubble-laden mixing layer with two-way coupling. J. Fluid Mech. 429, 23–61.

Elghobashi, S., Truesdell, G., 1993. On the two-way interaction between homogeneous turbulence and dispersed solid particles. I: turbulence modification. Phys. Fluids A 5 (7), 1790–1801.

Fukuta, M., Takagi, S., Matsumoto, Y., 2008. Numerical study on the shear-induced lift force acting on a spherical bubble in aqueous surfactant solutions. Phys. Fluids 20, 040704.

Gong, X., Takagi, S., Huang, H., Matsumoto, Y., 2007. A numerical study of mass transfer of ozone dissolution in bubble plumes with an Euler–Lagrange Method. Chem. Eng. Sci. 62, 1081–1093.

Hills, J.H., 1974. Radial non-uniformity of velocity and voidage in a bubble column. TransIChemE 52, 1–9.

Joshi, J.B., Vitankar, V.S., Kulkarni, A.A., Dhotre, M.T., Ekambara, K., 2002. Coherent flow structures in bubble column reactors. Chem. Eng. Sci. 57, 3157–3183.

Mazzitelli, I.M., Lohse, D., Toschi, F., 2003. On the relevance of the lift force in bubbly turbulence. J. Fluid Mech. 488, 283–313.

Morinishi, Y., Lund, S., Vasilyev, V., Moin, P., 1998. Fully conservative high order finite difference schemes for incompressible flow. J. Comp. Phys. 143 (1), 90–124.

Mudde, R., 2005. Gravity-driven bubbly flows. Ann. Rev. Fluid Mech. 37, 393–423.

Murai, Y., Matsumoto, Y., 1998. Numerical analysis of detailed flow structures of a bubble plume. JSME Int. J. Ser. B 41 (3), 568–574.

Oseen, C.W., 1910. Uber die Stokes'sche Formel und Uber eine verwandte Aufgabe in der Hydrodynamik. Ark Mat. Astron. Fys. 6 (29), 29–45.

Reid, R.C., Praunsnitz, J.M., Sherwood, T.K., 1977. The Properties of Gases and Liquids, third ed. McGraw-Hill, NY. p578.

Sander, R., 1999. Modeling atmospheric chemistry: interactions between gas-phase species and liquid cloud/aerosol particles. Surv. Geophys. 20, 1–31.

Sokolichin, A., Eigenberger, G., Lapin, A., 2004. Simulation of buoyancy driven bubbly flow: established simplifications and open questions. AIChE J. 50 (1), 24–45.

Spelt, P.D.M., Biesheuvel, A., 1997. On the motion of gas bubbles in homogeneous isotropic turbulence. J. Fluid Mech. 336, 221–244.

Squires, K.D., Eaton, J.K., 1990. Lagrangian and Eulerian statistics obtained from direct numerical simulations of homogeneous turbulence. Phys. Fluids A 3 (1), 130–143.

Takagi, S., Matsumoto, Y., 1996. Force acting on a spherical bubble rising through a quiescent liquid. Jpn. J. Multiphase Flows 10, 264–273 (in Japanese).

Takemura, F., Yabe, A., 1999. Rising speed and dissolution rate of a carbon dioxide bubble in slightly contaminated water. J. Fluid Mech. 378, 319–334.

Takemura, F., Magnaudet, J., 2004. The history force on a rapid shrinking bubble rising at finite Reynolds number. Phys. Fluids 16, 3247–3255.

Wilke, C.R., Chang, P., 1955. Correlation of diffusion coefficient in dilute solutions. AIChE J. 1, 264–270.

Zhang, Y., Finch, J.A., 2001. A note on single bubble motion in surfactant solutions. J. Fluid Mech. 429, 63–66.

Zhang, D., Prosperetti, Z.A., 1994. Averaged questions for inviscid disperse two-phase flow. J. Fluid Mech. 267, 185–219.